Article

Vacuum ultraviolet second-harmonic generation in $NH_4B_4O_6F$ crystal

https://doi.org/10.1038/s41586-025-10007-z

Received: 22 March 2025

Accepted: 4 December 2025

Published online: 28 January 2026

Check for updates

Fangfang Zhang[1,2,3], Zilong Chen[1,3], Chen Cui[1,3], Zhihua Yang[1,2], Miriding Mutailipu[1,2], Fuming Li[1], Xueling Hou[1], Xifa Long[1] & Shilie Pan[1,2]✉

Vacuum ultraviolet (VUV, 100–200 nm) light sources are crucial for advanced spectroscopy, quantum research and semiconductor lithography[1–3]. Compared with conventional large-scale VUV generation technologies[4–7], second-harmonic generation (SHG) through nonlinear optical (NLO) crystals[8–10] is the simplest and most efficient method. However, the scarcity of suitable NLO crystals has constrained the production of VUV light through SHG: existing materials fail to meet phase-matching requirements, suffer from low conversion efficiency or have severe growth limitations[11–19]. In this study, we report the development of the fluorooxoborate crystal $NH_4B_4O_6F$ (abbreviated as ABF) as a promising material for VUV light generation. VUV devices with specific phase-matching angles were constructed, achieving a record 158.9-nm light through phase-matching SHG and a maximum nanosecond pulse energy of 4.8 mJ at 177.3 nm with a conversion efficiency of 5.9%. The enhanced NLO performance is attributed to optimized arrangements of fluorine-based units creating asymmetric sublattices. This work provides further material in the NLO field, with potential for applications in compact, high-power VUV lasers using ABF.

Compact, efficient VUV light sources in the 100–200-nm range (corresponding to photon energies of 12.4–6.2 eV) are crucial for a wide range of applications, notably, advanced spectroscopy, quantum research and semiconductor lithography[1–3]. Compared with conventional large-scale VUV systems, including synchrotrons, free-electron lasers and large-scale gas-discharge sources[4–7], SHG, discovered in 1961, is the simplest and most efficient method for short-wavelength light generation through frequency-doubling in NLO crystals[8–10]. However, no conventional high-performance NLO crystals[11–14] satisfy birefringent phase-matching (BPM) in the VUV region, making them unsuitable for VUV SHG. Consequently, sum-frequency generation is often used as an alternative but suffers from higher complexity and lower efficiency than SHG, primarily because of the stringent temporal and spatial synchronization requirements between two distinct laser beams[15,16]. Alternatively, non-traditional phase-matching approaches, such as random quasi-phase-matching in SrB_4O_7, have been reported to generate coherent VUV radiation down to 121 nm, the shortest wavelength achieved through SHG in solid-state materials[17]. Yet the conversion efficiency is extremely low (approximately 4×10^{-5} at 160 nm) preventing it from meeting the high-power and high-stability demands of practical applications. $KBe_2BO_3F_2$ (KBBF), a benchmark NLO crystal developed in the 1990s, remains the only practical crystal that breaks the '200 nm wall' for VUV coherent light generation through BPM-SHG. Nevertheless, its layered growth habit induces a plate-like morphology along the *z*-axis, necessitating a specific prism-coupling technique to prevent cutting along the phase-matching direction and limiting conversion efficiency[18,19]. The quest for a suitable VUV NLO material with shorter output wavelengths, higher output energies and enhanced conversion efficiencies remains elusive despite continuing efforts.

Designing VUV NLO materials faces substantial challenges, including the combination of conflicting properties such as VUV transparency, strong NLO coefficient and substantial birefringence for phase-matching at VUV wavelengths. Critically, practical applications require high-quality single crystals with sufficient size for device fabrication, as well as stable physical and chemical properties, high laser-induced damage thresholds (LIDTs) and suitable hardness for processing[20,21]. Owing to these stringent requirements, no crystal has yet met all of these criteria simultaneously. Recently, we proposed a fluorination strategy by substituting fluorine for oxygen atoms in borates to regulate the structure and achieve balanced basic properties that are required for VUV applications in a series of fluorooxoborates[22,23]. Owing to the limitations of the preparation techniques for large-sized crystals, only preliminary performance assessments have been conducted on the basis of limited millimetre-scale crystals or polycrystalline powders[24,25]. In this work, we demonstrated the development and exceptional VUV NLO properties of ABF (ref. 24) by growing large single crystals with high quality, which show superior performances that hold great promise for practical applications. The fluorination effect on asymmetry and structure motif ordering that leads to performance enhancement is discussed.

[1]CAS Key Laboratory of Functional Materials and Devices for Special Environmental Conditions, Xinjiang Key Laboratory of Functional Crystal Materials, Xinjiang Technical Institute of Physics and Chemistry, Chinese Academy of Sciences, Urumqi, China. [2]Center of Materials Science and Optoelectronics Engineering, University of Chinese Academy of Sciences, Beijing, China. [3]These authors contributed equally: Fangfang Zhang, Zilong Chen, Chen Cui. ✉e-mail: slpan@ms.xjb.ac.cn

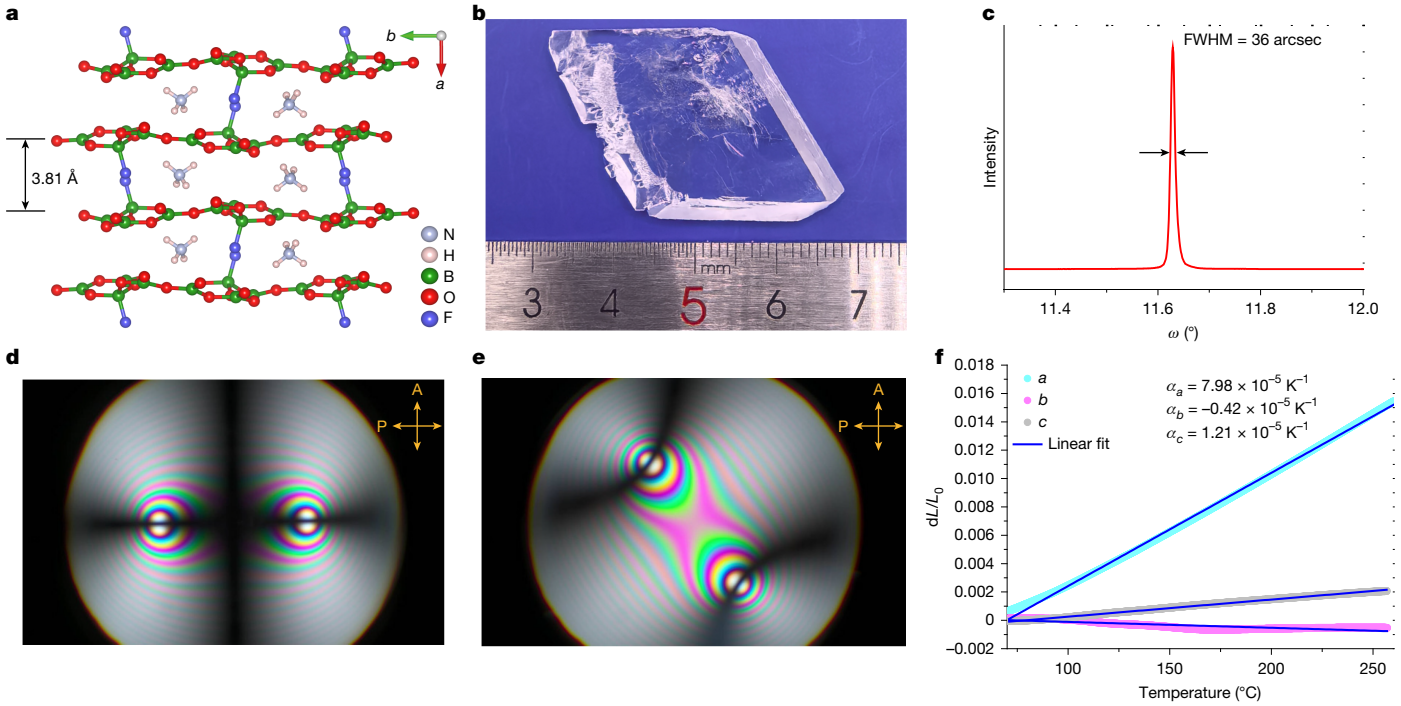

Fig. 1 | Structure, photograph, optical quality and thermal expansion properties of ABF. a, Structure of ABF featuring 2D $[B_4O_6F]_\infty$ layers with an interlayer distance of 3.81 Å. NH_4^+ cations are located between the layers, forming the final framework through hydrogen bonds (not shown for clarity). **b**, As-grown ABF crystal with centimetre-scale dimensions. **c**, X-ray rocking curve of ABF crystal. **d**,**e**, Convergent polarized light interference patterns of ABF crystal along the *b*-axis (**d**) and at a 45° angle to the *b*-axis (**e**). The polarization directions of the incident light (polarizer (P)) and the transmitted light (analyser (A)) are labelled. **f**, Thermal expansion measurements of ABF.

Crystal growth and optical quality of ABF

The structure of ABF features 2D $[B_4O_6F]_\infty$ layers interconnected by NH_4^+ cations through hydrogen bonds with an interlayer distance of 3.81 Å (ref. 24) (Fig. 1a), which is approximately half that of KBBF (6.25 Å)[18] (Extended Data Fig. 1). This key distinction endows ABF with a much higher interlayer binding energy than KBBF, which effectively mitigates the inherent prominent layered growth habit of KBBF and lays a structural foundation for growing thick ABF crystals[24]. Owing to its growth occurring in a multicomponent gas–liquid–solid three-phase environment, which makes conventional growth methods inefficient, the formation of large-size ABF crystals poses a considerable challenge. To address this, we devised an optimized vapour deposition method to produce large single crystals of ABF. In contrast to the conventional vapour transport deposition technique that typically requires ultrahigh vacuum conditions and a gas delivery system, our method operates under autogenous pressure without further transport agents (see details in Methods). Figure 1b presents the as-grown ABF crystal, which reaches centimetre-scale dimensions up to 25 × 18 × 10 mm^3. For the standard error and confidence interval (CI) for measured data with inherent measurement variability, see Methods. The X-ray rocking curve (Fig. 1c) exhibits a narrow full width at half maximum (FWHM) of 36 arcsec, indicating the high crystalline quality of the sample. The conoscopic interference patterns (Fig. 1d,e) unambiguously confirm that ABF is biaxial and that the as-grown crystal is optically homogeneous. The thermal expansion coefficients (Methods) for the *X*, *Y* and *Z* axes of ABF were measured using *a*-oriented, *c*-oriented and *b*-oriented crystal samples (Fig. 1f). Like LBO crystals, ABF exhibits positive expansion along the *X* and *Y* axes and negative expansion along the *Z* axis. However, its average thermal expansion coefficients ($\alpha_X = \alpha_a = 7.98 \times 10^{-5}$ K^{-1}, $\alpha_Y = \alpha_c = 1.21 \times 10^{-5}$ K^{-1} and $\alpha_Z = \alpha_b = -0.42 \times 10^{-5}$ K^{-1}) are much smaller than those of LBO ($\alpha_X = 10.1 \times 10^{-5}$ K^{-1}, $\alpha_Y = -7.1 \times 10^{-5}$ K^{-1} and $\alpha_Z = 3.1 \times 10^{-5}$ K^{-1})[26] (data from ref. 26, unit unified to 10^{-5} K^{-1}). The relatively small thermal expansion anisotropy of ABF helps to prevent cracking during crystal growth and processing. Mechanical hardness measurement (Methods) on a (100) plate of ABF shows a Vickers hardness of 201 HV (HV0.3, 10 s dwell time), corresponding to a moderate Mohs hardness of about 4, which facilitates processing.

High performance as a practical VUV NLO crystal

ABF stands out as such a practical VUV NLO crystal, with key advantages outlined here. First, it has excellent VUV transparency—a critical property for VUV-related applications. Notably, ABF features a wide transparency region spanning from VUV to near-infrared (Fig. 2a). Its UV cut-off edge extends down to 155 nm, enabling high transmittance across several VUV wavelengths, specifically 177.3 nm (sixth-harmonic generation of 1,064-nm Nd:YAG laser) and 193 nm (output wavelength of an ArF excimer laser), both critical for high-resolution photoelectron spectroscopy and photolithography applications. Second, ABF exhibits suitable birefringence and chromatic dispersion to achieve phase-matching at VUV wavelengths. Its wavelength-dependent refractive indices were determined using the minimum deviation method and subsequently fitted using Sellmeier equations (Fig. 2b). We confirmed that ABF is an optically negative biaxial crystal with the relationship $n_z - n_y < n_y - n_x$. Furthermore, type I phase-matching curves for SHG were evaluated, showing that the shortest phase-matching SHG wavelength (λ_{SH}) of ABF in the *X*–*Y* plane is 158 nm (Fig. 2c). Among all known crystals with λ_{SH} below 200 nm that are confirmed through refractive index measurements and dispersion equation fitting[18,25,27–31], ABF holds the distinction of having the shortest λ_{SH}. We noticed that other potential candidates, for example, γ-BBF (ref. 28), with theoretically predicted VUV NLO performance superior to KBBF, urgently face challenges in large-scale single-crystal growth and experimental verification. Third, ABF delivers a strong SHG response, which is essential for high conversion efficiency in the VUV region. ABF crystallizes in the space group $Pna2_1$ (point group *mm*2) and exhibits three non-zero independent second-order NLO coefficients: d_{31}, d_{32} and d_{33}. For type I SHG (o + o → e)

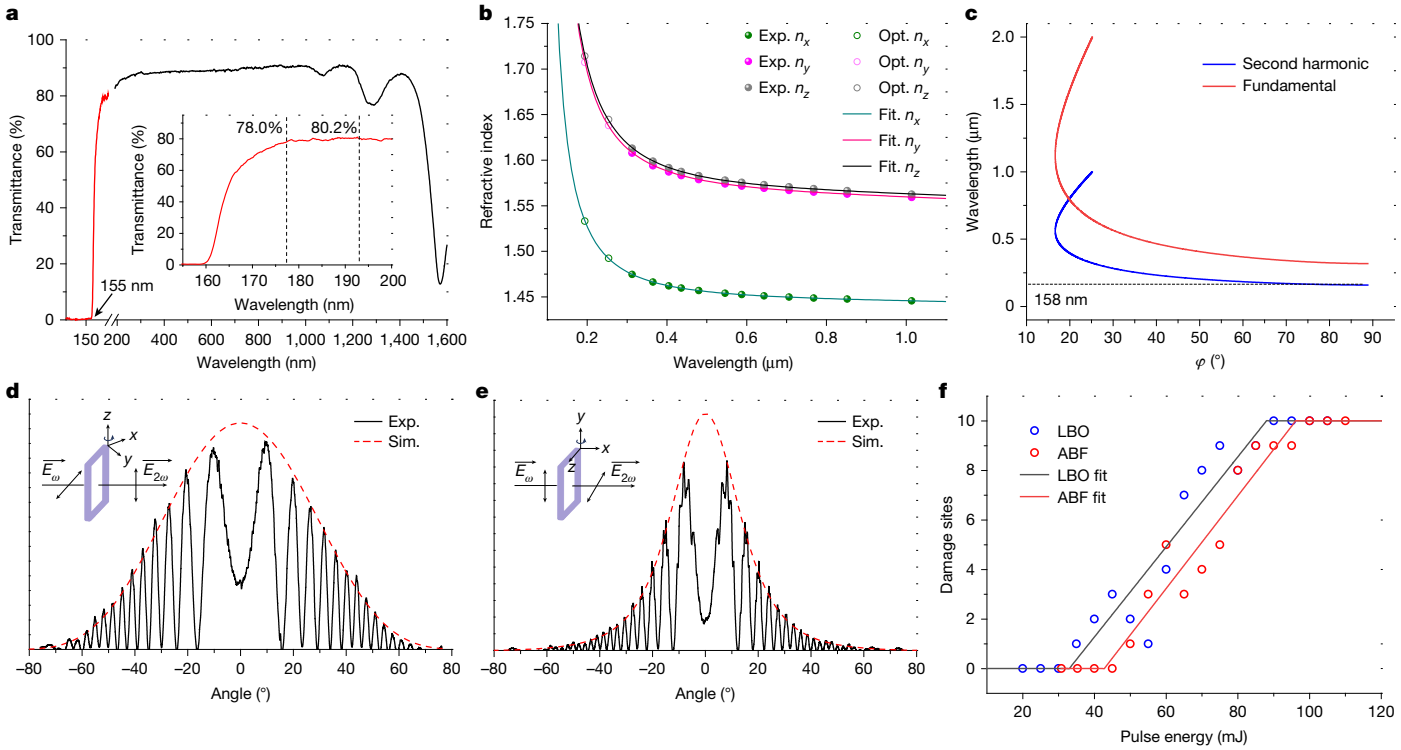

Fig. 2 | Characterizations of ABF. a, Transmission spectra of ABF in the 155–1,600-nm region. Inset, transmission spectrum in the 155–200-nm region. Notable transmittance values include 0.5% at UV cut-off edge of 155 nm, 78.0% at 177.3 nm and 80.2% at 193.0 nm. **b**, Refractive index dispersion curves of ABF. **c**, Type I phase-matching curves of the SHG process in the *X*–*Y* plane for ABF. **d**,**e**, SHG measurements using the Maker fringe technique. Shown are the measured and calculated Maker fringe data and fitted envelopes for d_{36} of the benchmark crystal KDP (**d**) and d_{32} of ABF (**e**). Insets, measurement configurations for KDP ($\theta = 90°$, $\varphi = 45°$) and ABF ($\theta = 90°$, $\varphi = 0°$). **f**, Comparative LIDT measurements between ABF and reference LBO crystals. At each pulse-energy setting, the sample was irradiated 10 times at fresh sites and the number of damaged sites was recorded.

in the *X*–*Y* plane, the effective second-order NLO coefficient (d_{eff}) is expressed as $d_{eff} = d_{32}\cos\varphi$, in which φ denotes the azimuthal angle[20]. Thus, we measured the d_{32} coefficient of ABF for SHG (1,064 → 532 nm) using the Maker fringe technique, yielding a value of 1.09 pm V^{-1} (Fig. 2d,e). Furthermore, the phase-matching harmonic-generation method, conducted under conditions closer to practical applications, shows a d_{32} value of 0.93 pm V^{-1}. Both measurements identify that ABF has an extremely large second-order NLO coefficient. The advantage of the SHG response of ABF is even more pronounced in the VUV region. Assuming weak wavelength dependence of the NLO coefficients d_{ij} far from the cut-off edge, we deduced d_{eff} across the entire phase-matching range. The results show that the d_{eff} of ABF is consistently much larger than that of KBBF. Specifically, at 386 → 193 nm and 355 → 177.5 nm, the d_{eff} values of ABF are 0.63 and 0.48 pm V^{-1}, respectively, much higher than the corresponding values of KBBF (0.26 and 0.20 pm V^{-1}) at these wavelengths[32,33] (see Extended Data Fig. 2 for details). The larger d_{eff} makes ABF more conducive to achieving higher laser conversion efficiency, supporting the development of more efficient, high-power laser systems. Fourth, ABF exhibits a high LIDT. Figure 2f presents LIDT measurement results for ABF, with LBO (ref. 34)—the established commercial NLO crystal with exceptional laser-damage resistance—serving as a reference. ABF demonstrates a superior LIDT of 1.6 GW cm^{-2}, exceeding that of LBO of 1.2 GW cm^{-2} (1,064 nm, 8 ns, one-on-one testing), highlighting its strong potential for high-power laser applications. Detailed protocols for measuring transmittance, refractive indices, SHG coefficients and LIDTs are provided in Methods.

Tunable high-efficiency frequency doubling

Tunable frequency-doubled light outputs were achieved from 158.9 to 340.2 nm. Figure 3 illustrates the experimental set-up and detection of frequency-doubling light spanning 158.9–188.0 nm (Fig. 3a), using an ABF device aligned at (θ, φ) = (90°, 70°). Further frequency-doubling measurements for 190.4–230.5 nm (device: (θ, φ) = (90°, 40°)) and 255.1–340.2 nm (device: (θ, φ) = (90°, 0°)) are provided in Extended Data Figs. 3–6. The shortest experimentally achieved phase-matching SHG output at 158.9 nm surpasses the previous world record of 165 nm held by KBBF crystal[19]. This breakthrough opens new possibilities in fields such as the study of superconducting mechanisms (in which higher photon energies enable a larger observable Brillouin zone, providing critical insights into superconductors)[35] and photochemical investigations (in which VUV sources can be used to examine chemical reactions, as the energy of numerous chemical bonds falls within this wavelength range)[36,37].

Then we fabricated SHG devices for the 354.7 → 177.3 nm transition to test the frequency-doubling ability of ABF (Fig. 4). This device circumvents the energy loss inherent in the CaF_2 or SiO_2 prisms used in the prism-coupled devices of KBBF (Fig. 4a). Output energies at 177.3 nm were recorded for various input energies at 354.7 nm, with the results shown in Fig. 4b. An output energy of 4.8 mJ was achieved at a pump energy of 81.0 mJ, corresponding to an SHG conversion efficiency of 5.9%, with a maximum efficiency of 7.9% at 28.0 mJ. These values greatly exceed those of KBBF under nanosecond pulse conditions (0.375 mJ output energy and 1.76% conversion efficiency)[38]. It is worth noting that, since the invention of laser technology in 1960, many potential NLO crystals have been reported, but no new crystals have achieved a 177.3-nm SHG output through BPM, except for KBBF prism-coupled devices. ABF not only realizes this output but also delivers the highest nanosecond-pulse SHG energy output and conversion efficiency so far. Of course, it is anticipated that both the output energy and conversion efficiency could be further improved in future work through improved crystal quality and device-fabrication precision.

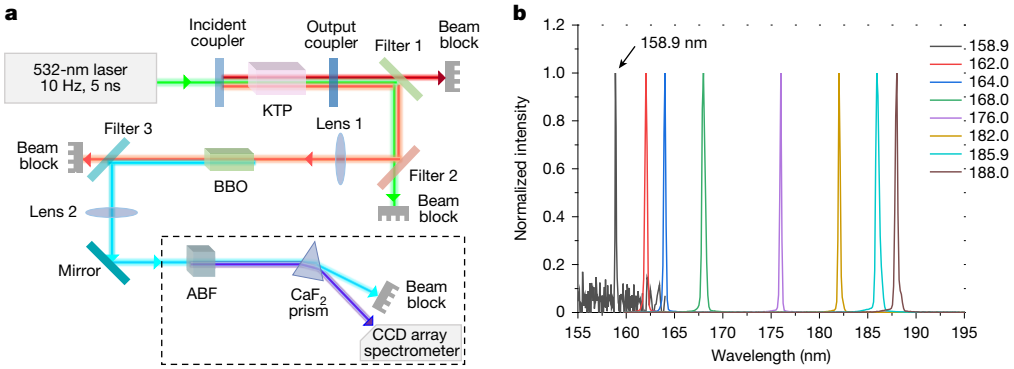

Fig. 3 | Tunable frequency-doubling output of ABF. a, Schematic of the set-up for tunable VUV generation using ABF crystal. The system includes a 532-nm pump laser (10 Hz, 5 ns) driving a KTP-OPO (620–720-nm tunable signals), a BBO crystal (for frequency-doubling to 310–360-nm fundamental light), a convex–concave telescope system (beam collimation, focusing and spatial optimization), an ABF crystal (VUV generation), a Brewster's angle-cut CaF_2 prism (splitting UV and VUV beams) and an argon-filled glovebox (dashed lines, VUV generation environment). Arrowed solid lines indicate the optical path. See Methods for detailed experimental procedures. **b**, Observation of frequency-doubling light for 158.9–188.0 nm using an ABF device with $(\theta, \varphi) = (90°, 70°)$. Note that 158.9 nm is close to the shortest phase-matching wavelength limit of the ABF crystal, with relatively low signal-to-noise ratio at this wavelength; the SHG intensity is normalized for clarity and raw data are presented in Extended Data Fig. 3.

Fluorination effect on asymmetry and motif ordering

NLO performance is determined primarily by the chemical composition and electronic structure of local atomic groups. Traditional basic units in borate NLO materials are $[BO_3]$ and $[BO_4]$; $[BO_4]$ is rarely preferred owing to unfavourable optical responses[39], whereas non-condensed $[BO_3]$ contains dangling bonds that hinder large bandgaps, leaving few pure $[BO_3]$-based borates suitable for VUV NLO applications. By contrast, ABF contains both $[BO_3]$ and $[BO_3F]$ groups; the introduction of the $[BO_3F]$ unit is beneficial for the full breakthrough of ABF in the NLO field. Compared with the T_d symmetry of the ideal $[BO_4]$ tetrahedron, $[BO_3F]$ exhibits lower symmetry (C_{3v}), which inherently induces asymmetric electron density distribution. Specifically, the Mayer bond order of B–O and B–F bonds in $[BO_3F]$ are approximately 1.28 and 0.63, respectively, with the bond order of B–O being nearly twice that of B–F. A comparison of the Laplacian charge density between $[BO_3F]$ and $[BO_4]$ units confirms the inequivalent covalent interactions in $[BO_3F]$, which greatly favours optical performances (Extended Data Fig. 7). Analysis of the sublattice symmetry of ABF reveals the absence of inversion centres for the B and O/F sublattices within the unit cell, confirming the non-centrosymmetric nature of ABF ($Pna2_1$; Fig. 5a). Symmetry-adapted Wannier function calculations[40,41] show that SHG contributions originate primarily from the associated orbitals in the B and O/F sublattices, highlighting the role of non-centrosymmetric sublattice band-edge orbitals. Specifically, the B and O/F orbitals contribute more than 77% to SHG response (Extended Data Table 1).

As a bond terminator, fluorine 'cut' the B–O framework to modulate the anionic skeleton, enabling the formation of two-dimensional anionic layers. As illustrated in Fig. 5b, ABF exhibits anionic layers with a thickness of 0.75 Å (defined as the maximum vertical distance between B atom centres along the *a*-axis), in contrast to the three-dimensional anionic framework of $NH_4B_5O_8$, which lacks such fluorine-induced regulation (Extended Data Fig. 8). In ABF, the $[BO_3F]$ units regulate the motif ordering to achieve a high degree of polymerization. Notably, the highly oriented arrangement of polymerized anionic groups in the layered structure of ABF facilitates the effective superposition of the polarization anisotropy of $[BO_3]$ and $[BO_3F]$ units (Fig. 5c), which enhances birefringence and phase-matching capability of ABF. Furthermore, the high polymerization of $[BO_3]$ and $[BO_3F]$ drives the elimination of the dangling bonds of oxygen atoms. Therefore, the introduction of $[BO_3F]$, the core of the fluorination effect, drives the superior performances of ABF: it modulates asymmetry, structural motif ordering and anionic framework structure, facilitates polymerization and oriented arrangement and ultimately boosts properties including VUV transmission, large birefringence and an enhanced NLO response.

Conclusion

We report ABF, a fluorooxoborate crystal, as a transformative solution to the long-standing challenge of developing practical VUV NLO materials. ABF resolves key limitations of existing systems, most notably the layered growth habit of the benchmark crystal KBBF, while delivering exceptional performance across metrics critical for VUV lasing through SHG.

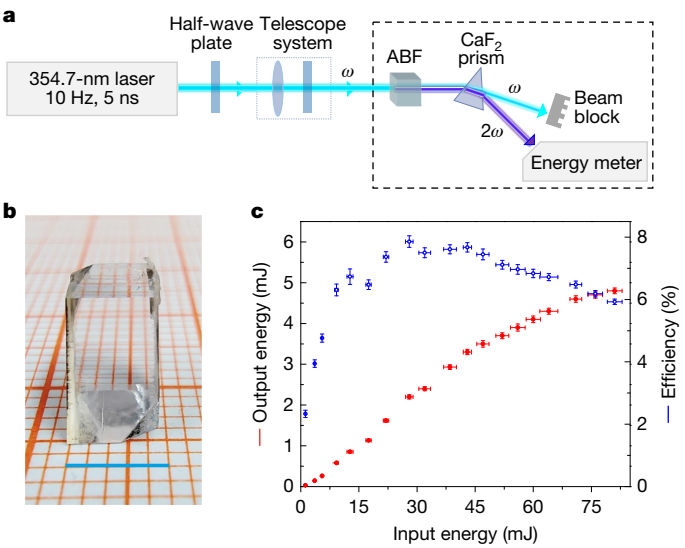

Fig. 4 | High-efficiency frequency-doubling output of ABF. a, Schematic of the set-up for 177.3-nm high-energy VUV nanosecond laser generation in ABF. The system includes a 354.7-nm third-harmonic fundamental laser (10 Hz, 5 ns), a convex–concave telescope system (beam optimization to about 4 mm × 6 mm (minor × major)), an ABF crystal (mounted in an argon-filled glovebox, dashed lines, for orientation adjustment) and a Brewster's angle-cut CaF_2 prism (splitting 354.7-nm incident and 177.3-nm generated VUV beams). Arrowed solid lines indicate the optical path. See Methods for detailed experimental procedures. **b**, Device fabricated with phase-matching angle for SHG at 354.7 → 177.3 nm. Scale bar, 5 mm. **c**, Output energy and conversion efficiency for SHG at 354.7 → 177.3 nm. Data points are means of repeated measurements; error bars indicate 95% CIs based on 100 measurements for output energy and 10 measurements for input energy.

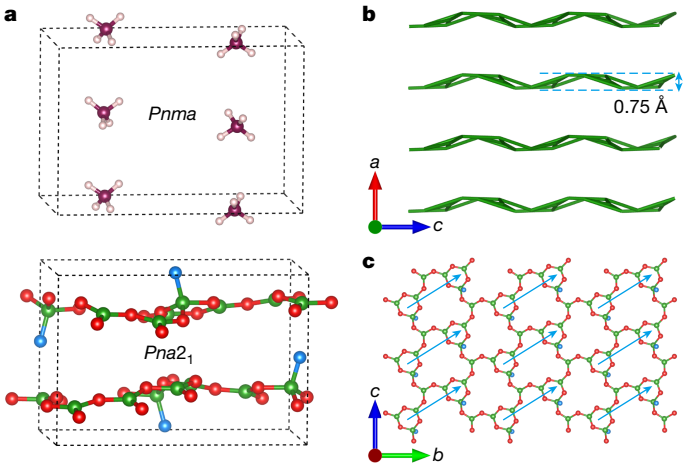

Fig. 5 | Theoretical analysis. a, Symmetry of the sublattice in ABF, in which the sublattice of NH_4^+ (top) belongs to the centrosymmetric *Pnma* space group and the sublattice of B–O/F (bottom) belongs to the non-centrosymmetric *Pna*2$_1$ space group. **b**, Topological view of the two-dimensional anionic layers of ABF (thickness: 0.75 Å). **c**, Arrangement of polymerized anionic groups in the layered structure of ABF. The blue lines represent the high-orientation arrangement of microscopic groups.

A comparative summary of ABF and KBBF (Extended Data Table 2) directly highlights the advantages of ABF in both core performance and practicality. Notably, ABF can generate high-power VUV light through SHG without relying on a prism-coupling technique. It exhibits excellent comprehensive performance, including a short UV cut-off edge, a broad phase-matching range, a largely effective SHG coefficient and an extremely high LIDT supporting high-power operation. For practical SHG devices, ABF achieves two pivotal milestones: the shortest VUV wavelength (158.9 nm) ever generated through birefringent phase-matching SHG in bulk crystal and a maximum pulse energy of 4.8 mJ at 177.3 nm, accompanied by a high SHG conversion efficiency of 5.9%. The introduction of fluorine to form asymmetric [BO_3F] with inequivalent covalent interactions drives the motif ordering and realizes fully upgraded NLO performances. The full breakthrough of ABF paves the way for compact, efficient all-solid-state VUV lasers, which will accelerate widespread applications of VUV light in contemporary science (for example, high-resolution superconducting spectroscopy) and industry (for example, 193-nm semiconductor lithography), marking a transformative step in VUV photonics.

Online content

Any methods, additional references, Nature Portfolio reporting summaries, source data, extended data, supplementary information, acknowledgements, peer review information; details of author contributions and competing interests; and statements of data and code availability are available at https://doi.org/10.1038/s41586-025-10007-z.

1. Eaton, D. F. Nonlinear optical materials. *Science* **253**, 281–287 (1991).
2. Meng, J. Q. et al. Design and synthesis of an ultraviolet-transparent nonlinear optical crystal $Sr_2Be_2B_2O_7$. *Nature* **373**, 322–324 (1995).
3. Cyranoski, D. China's crystal cache. *Nature* **457**, 953–955 (2009).
4. Weinert, T. et al. Proton uptake mechanism in bacteriorhodopsin captured by serial synchrotron crystallography. *Science* **365**, 61–65 (2019).
5. Samson, J. A. & Ederer, D. L. *Vacuum Ultraviolet Spectroscopy* (Academic Press, 2000).
6. Basting, D. & Marowsky, G. *Excimer Laser Technology* (Springer, 2005).
7. O'Shea, P. G. & Freund, H. P. Free-electron lasers: status and applications. *Science* **292**, 1853–1858 (2001).
8. Franken, P. A., Hill, A. E., Peters, C. W. & Weinreich, G. Generation of optical harmonics. *Phys. Rev. Lett.* **7**, 118–119 (1961).
9. Bloembergen, N. *Nonlinear Optics* (World Scientific, 1996).
10. Boyd, R. W. *Nonlinear Optics* (Academic Press, 2008).
11. Eimerl, D. Electro-optic, linear, and nonlinear optical properties of KDP and its isomorphs. *Ferroelectrics* **72**, 95–139 (1987).
12. Chen, C. T., Wu, B. C., Jiang, A. D. & You, G. M. A new-type ultraviolet SHG crystal β-BaB_2O_4. *Sci. Sin. B* **18**, 235–243 (1985).
13. Chen, C. T. et al. New nonlinear-optical crystal: LiB_3O_5. *J. Opt. Soc. Am. B* **6**, 616–621 (1989).
14. Mori, Y., Kuroda, I., Nakajima, S., Sasaki, T. & Nakai, S. New nonlinear optical crystal: cesium lithium borate. *Appl. Phys. Lett.* **67**, 1818–1820 (1995).
15. Mirov, S. B., Fedorov, V. V., Boczar, B., Frost, R. & Pryor, B. All-solid-state laser system tunable in deep ultraviolet based on sum-frequency generation in CLBO. *Opt. Commun.* **198**, 403–406 (2001).
16. Zhang, Z. T. et al. High-power, narrow linewidth solid-state deep ultraviolet laser generation at 193 nm by frequency mixing in LBO crystals. *Adv. Photonics Nexus* **3**, 026012 (2024).
17. Trabs, P., Noack, F., Aleksandrovsky, A. S., Zaitsev, A. I. & Petrov, V. Generation of coherent vacuum UV radiation in randomly quasi-phase-matched strontium tetraborate. In *Proc. 2015 Conference on Lasers and Electro-Optics (CLEO)* https://doi.org/10.1364/CLEO_SI.2015.STh3H.2 (IEEE, 2015).
18. Wu, B. C., Tang, D. Y., Ye, N. & Chen, C. T. Linear and nonlinear optical properties of the $KBe_2BO_3F_2$ (KBBF) crystal. *Opt. Mater.* **5**, 105–109 (1996).
19. Dai, S. B. et al. 2.14 mW deep-ultraviolet laser at 165 nm by eighth-harmonic generation of a 1319 nm Nd:YAG laser in KBBF. *Laser Phys. Lett.* **13**, 035401 (2016).
20. Chen, C. T. et al. *Nonlinear Optical Borate Crystals: Principles and Applications* (Wiley, 2012).
21. Nikogosyan, D. N. *Nonlinear Optical Crystals: A Complete Survey* (Springer, 2009).
22. Zhang, B. B., Shi, G. Q., Yang, Z. H., Zhang, F. F. & Pan, S. L. Fluorooxoborates: beryllium-free deep-ultraviolet nonlinear optical materials without layered growth. *Angew. Chem. Int. Ed.* **56**, 3916–3919 (2017).
23. Mutailipu, M., Zhang, M., Yang, Z. H. & Pan, S. L. Targeting the next generation of deep-ultraviolet nonlinear optical materials: expanding from borates to borate fluorides to fluorooxoborates. *Acc. Chem. Res.* **52**, 791–801 (2019).
24. Shi, G. Q. et al. Finding the next deep-ultraviolet nonlinear optical material: $NH_4B_4O_6F$. *J. Am. Chem. Soc.* **139**, 10645–10648 (2017).
25. Wang, X. F. et al. CsB_4O_6F: a congruent-melting deep-ultraviolet nonlinear optical material by combining superior functional units. *Angew. Chem. Int. Ed.* **56**, 14119–14123 (2017).
26. Shepelev, Y. F., Bubnova, R. S., Filatov, S. K., Sennova, N. A. & Pilneva, N. A. LiB_3O_5 crystal structure at 20, 227 and 377 °C. *J. Solid State Chem.* **178**, 2987–2997 (2005).
27. Chen, C. T. et al. Deep UV nonlinear optical crystal: $RbBe_2(BO_3)F_2$. *J. Opt. Soc. Am. B* **26**, 1519–1525 (2009).
28. Peng, G. et al. $NH_4Be_2BO_3F_2$ and γ-Be_2BO_3F: overcoming the layering habit in $KBe_2BO_3F_2$ for the next-generation deep-ultraviolet nonlinear optical materials. *Angew. Chem. Int. Ed.* **57**, 8968–8972 (2018).
29. Liu, H. N. et al. $Cs_3[(BOP)_2(B_3O_7)_3]$: a deep-ultraviolet nonlinear optical crystal designed by optimizing matching of cation and anion groups. *J. Am. Chem. Soc.* **145**, 12691–12700 (2023).
30. Zou, G. H. et al. Alkaline-alkaline earth fluoride carbonate crystals $ABCO_3F$ (A = K, Rb, Cs; B = Ca, Sr, Ba) as nonlinear optical materials. *J. Am. Chem. Soc.* **133**, 20001–20007 (2011).
31. Mutailipu, M. et al. Achieving the full-wavelength phase-matching for efficient nonlinear optical frequency conversion in $C(NH_2)_3BF_4$. *Nat. Photonics* **17**, 694–701 (2023).
32. Chen, C. T., Wang, G. L., Wang, X. Y. & Xu, Z. Y. Deep-UV nonlinear optical crystal $KBe_2BO_3F_2$—discovery, growth, optical properties and applications. *Appl. Phys. B* **97**, 9–25 (2009).
33. Li, R., Wang, L. R., Wang, X. Y., Wang, G. L. & Chen, C. T. Dispersion relations of refractive indices suitable for $KBe_2BO_3F_2$ crystal deep-ultraviolet applications. *Appl. Opt.* **55**, 10423–10426 (2016).
34. Liu, H. J., Wang, F., Sun, L. X., Zheng, T. R. & Wang, F. R. Laser damage properties of LiB_3O_5 crystal surface under UV laser irradiation. *Opt. Express* **31**, 30184–30193 (2023).
35. Berntsen, M. H., Gotberg, O. & Tjernberg, O. An experimental setup for high resolution 10.5 eV laser-based angle-resolved photoelectron spectroscopy using a time-of-flight electron analyzer. *Rev. Sci. Instrum.* **82**, 095113 (2011).
36. Chang, Y. C., Xiong, B., Bross, D. H., Ruscic, B. & Ng, C. Y. A vacuum ultraviolet laser pulsed field ionization-photoion study of methane (CH_4): determination of the appearance energy of methylium from methane with unprecedented precision and the resulting impact on the bond dissociation energies of CH_4 and CH_4^+. *Phys. Chem. Chem. Phys.* **19**, 9592–9605 (2017).
37. Cao, W., Laurent, G., Ben-Itzhak, I. & Cocke, C. L. Identification of a previously unobserved dissociative ionization pathway in time-resolved photospectroscopy of the deuterium molecule. *Phys. Rev. Lett.* **114**, 113001 (2015).
38. Wen, N. et al. Generation of a 177.3 nm VUV laser with high pulse energy by a KBBF crystal. *Laser Phys. Lett.* **17**, 105001 (2020).
39. Chen, C. T., Wu, Y. C. & Li, R. K. The anionic group theory of the non-linear optical effect and its applications in the development of new high-quality NLO crystals in the borate series. *Int. Rev. Phys. Chem.* **8**, 65–91 (1989).
40. Lei, B. H., Pan, S. L., Yang, Z. H., Cao, C. & Singh, D. J. Second harmonic generation susceptibilities from symmetry adapted Wannier functions. *Phys. Rev. Lett.* **125**, 187402 (2020).
41. Li, F. M. et al. Covalently bonded fluorine optimizing deep-ultraviolet nonlinear optical performance of fluorooxoborates. *Sci. Bull.* **69**, 1192–1196 (2024).

Methods

Synthesis and crystal growth

Polycrystalline samples of ABF were prepared by a conventional high-temperature solid-state reaction method in a closed system. A stoichiometric mixture of NH_4F and B_2O_3 was sealed in an autoclave equipped with a platinum liner. The autoclave was heated to 360 °C in 24 h, held at this temperature for two days and then cooled to room temperature in 24 h. Single crystals of ABF were grown by an optimized vapour deposition method. Polycrystalline samples of ABF were sealed in an autoclave equipped with a platinum liner. The autoclave was put in a vertical-tube furnace equipped with heating element of resistance wire. By meticulously designing the temperature gradient, nucleation is facilitated, thereby promoting the growth of a singular, large crystal.

X-ray rocking curve

X-ray rocking curves were acquired on a Bruker D8 Advance X-ray diffractometer (Cu $K\alpha_1$ radiation, $\lambda = 1.5406$ Å). Measurements were conducted in ω-scan mode under a generator voltage of 40 kV and a generator current of 40 mA and the diffractometer featured an angular precision of 0.0001°. The (100) crystal plane of ABF was used and the result shows a FWHM of 36.0 ± 0.7 arcsec (95% CI: 35.6–36.6 arcsec).

Transmittance spectra

Transmittance spectra were measured on (100) plates without coatings. Data in the wavelength range from 200 to 1,600 nm were detected on a 2.3-mm-thick plate by SolidSpec-3700DUV spectrophotometer in a nitrogen gas atmosphere. Data in the wavelength range from 155 to 200 nm were detected on a 0.05-mm-thick plate by Metrolux ML6500 VUV spectrophotometer under vacuum conditions.

LIDT

The LIDT measurements were conducted in accordance with the ISO 21254-2:2011 standard using the one-on-one test methodology[42]. The laser source used was a pulsed Q-switched Nd:YAG laser, which emits a Gaussian-shaped pulse with a duration of 8 ns (FWHM at 1,064 nm), operating at a repetition rate of 1 Hz to avoid thermal accumulation. Laser pulses were focused onto the sample surface by means of a plano-convex lens (focal length: 150 mm) to form a circular spot with a diameter of 0.64 mm (measured using the knife-edge method); laser pulse energy was adjustable in the range 20–120 mJ and real-time-calibrated using a laser energy meter. The measurement was carried out on a (100)-oriented ABF plate and the phase-matching LBO crystal for UV SHG (700 → 350 nm) was measured as a reference. The damage probability was plotted as a function of the fluence and the data were linearly extrapolated to determine the fluence at which the damage probability is zero, yielding the LIDT value. Specifically, the LIDT of ABF was determined to be 1.6 ± 0.2 GW cm^{-2} (95% CI: 1.2–2.0 GW cm^{-2}), whereas the LIDT of the reference LBO crystal was 1.2 ± 0.2 GW cm^{-2} (95% CI: 0.8–1.6 GW cm^{-2}).

Thermal expansion coefficients

Thermal expansion coefficients for the *X*, *Y* and *Z* axes of ABF were measured by a NETZSCH DIL 402 PC dilatometer. The measurements were conducted under an air atmosphere over a temperature range of 70–260 °C and a heating rate of 5 °C min^{-1}. Before the measurements, the instrument was calibrated using standard sapphire samples. The ABF sample used was a rectangular prism, with faces perpendicular to the principal crystal axes and edge lengths of 4.42 mm, 4.62 mm and 3.47 mm, respectively. Figure 1f shows that the thermal expansion ratio of ABF is almost linear over the entirely measured temperature range from 70 to 260 °C and it exhibits positive expansion along the *X* and *Y* axes and negative expansion along the *Z* axis. The mean linear thermal expansion coefficients in the measured temperature range were calculated according to the thermal expansion ratio curves: $\alpha_X = \alpha_a = 7.98 \times 10^{-5}$ K^{-1} (standard error (SE) = 7.29×10^{-8} K^{-1}, 95% CI: [7.97×10^{-5}, 7.99×10^{-5}] K^{-1}), $\alpha_Y = \alpha_c = 1.21 \times 10^{-5}$ K^{-1} (SE = 1.40×10^{-8} K^{-1}, 95% CI: [1.21×10^{-5}, 1.21×10^{-5}] K^{-1}) and $\alpha_Z = \alpha_b = -0.42 \times 10^{-5}$ K^{-1} (SE = 6.52×10^{-8} K^{-1}, 95% CI: [-0.43×10^{-5}, -0.41×10^{-5}] K^{-1}).

Mechanical hardness

The Vickers hardness measurements were performed using a DHV-1000 microhardness meter under the conditions of HV0.3 (0.3 kgf test load) and 10 s dwell time. Five non-overlapping measurement points were selected, yielding individual hardness values of 201, 203, 198, 200 and 203 HV. The result was calculated as 201 ± 1 HV (95% CI: 198–204 HV). Mohs hardness (HM) was calculated from Vickers hardness (HV) using the following equation: $HM = 0.675(HV)^{1/3}$.

Refractive indices

Refractive indices were measured using the standard method of minimum deviation[43] on a SpectroMaster UV–Vis–IR spectrophotometer (Trioptics). Two prisms of ABF with apex angles of about 20° and different cutting orientations were used. The measurements were performed on 12 different monochromatic sources across a broad wavelength range from 253 to 1,013 nm. n_x, n_y and n_z represent the refractive index along the *a*-axis, *c*-axis and *b*-axis, respectively. The accuracy of the measurements is estimated to be 1×10^{-5}. Subsequently, the refractive indices were fitted by Sellmeier equations $n_i^2 = A + \frac{B}{\lambda^2 - C} - D \times \lambda^2$, in which λ is the wavelength (the unit of λ is μm) and A–D are the parameters[44]. Also, the Sellmeier equations were further optimized on the basis of the phase-matching angles obtained during the runnable SHG output experiments in the range 158.9–235 nm. This optimization provides a relatively accurate refractive index dispersion equation for ABF over a wide range extending from the VUV to the near-infrared spectral region.

Second-order nonlinear coefficient

The second-order nonlinear coefficient d_{32} of ABF was determined by means of two distinct methods. For the Maker fringe technique[45,46], the fundamental optical source used is a Q-switched Nd:YAG laser operating at a wavelength of 1,064 nm, with a repetition rate of 100 Hz, a pulse width of 10 ns, a maximum energy of 40 mJ and a TEM_{00} transverse mode. The second-harmonic signal, varying with crystal rotation angle, was detected by a photomultiplier tube, averaged using a fast-gated integrator and boxcar averager (Stanford Research Systems) and recorded by a computer. The system schematic and calculations were reported elsewhere[47]. An ABF crystal ($\theta = 90°$, $\varphi = 0°$) was used for measurements, with a KDP crystal ($\theta = 90°$, $\varphi = 45°$) as a reference. The KDP crystal was rotated on the *X*–*Y* plane with *Z* as the axis, whereas the ABF crystal was rotated on the *X*–*Z* plane with *Y* as the axis. The simulated envelopes (dashed red line in Fig. 2d,e) indicate that d_{32} of ABF is 2.8 times larger than that of KDP ($d_{36} = 0.39$ pm V^{-1}), corresponding to 1.09 pm V^{-1}.

Phase-matching measurements were conducted using a high-power pulsed laser operating at 1,064 nm, featuring a pulse duration of approximately 5 ns, a repetition rate of 40 kHz and a maximum power output of 40 W. The laser beam was focused to a diameter of about 400 μm at the waist using a lens with a focal length of 750 mm. A LBO crystal ($\theta = 90°$, $\varphi = 11.3°$) with anti-reflective coating at 1,064 nm and 532 nm and an ABF crystal ($\theta = 90°$, $\varphi = 0°$) with no coating were used to measure the output power of SHG from 1,064 to 532 nm at phase-matching orientations. These crystals were successively positioned at the waist of the 1,064-nm laser beam. At a pump power of 20 W, the output powers of ABF and the referenced LBO crystals were 127 and 120 mW, respectively, which reveals a value of 0.93 pm V^{-1} for d_{32} of ABF.

Tunable and high-efficiency frequency-doubling output of ABF

Tunable nanosecond harmonic light generation. The experimental set-up for generating tunable 158.9–230.5-nm light is shown in

Fig. 3, which comprises a 532-nm green laser pump with a pulse duration of 5 ns and a repetition rate of 10 Hz, capable of delivering a maximum pulse energy of 100 mJ. The optical parametric oscillator (OPO) signal is tunable from 620 to 940 nm by means of KTP crystals. The frequency-doubling of the KTP-OPO signal by a BBO crystal serves as the fundamental laser for subsequent SHG of the ABF crystal. Owing to the excessively broad bandwidth of the KTP-OPO signal, the energy output of the tunable UV laser is less than 2.0 mJ. The UV beam is collimated by lens 2, focused by lens 3 onto the ABF crystal positioned at the focal point and spatially optimized to a diameter of about 1 mm using a convex–concave telescope system. By adjusting the ABF orientation and the wavelengths of the KTP-OPO signals and BBO-SHG to satisfy phase-matching conditions, the ABF-SHG output was detected with a CCD array spectrometer. A CaF_2 prism, angled at Brewster's angle, splits the fundamental UV beam and the VUV signal. All operations for generating the VUV signal were conducted in an argon-filled glovebox environment to minimize atmospheric absorption.

Generation of high-energy 177.3-nm nanosecond laser in ABF. The experimental configuration is depicted in Fig. 4. The fundamental laser is a third-harmonic laser emitting at 354.7 nm with a pulse duration of 5 ns and a repetition rate of 10 Hz. Beam optimization is achieved through a telescope system comprising a convex and concave lens, minimizing the beam size before its incidence onto the ABF crystal. The laser beam is approximately 4 mm × 6 mm (minor × major). In an argon-filled glovebox, VUV laser generation is facilitated by adjusting the orientation of the ABF crystal. A CaF_2 prism, cut at Brewster's angle and positioned behind the ABF crystal, splits the incident laser at 354.7 nm and the generated laser at 177.3 nm.

First-principles calculations

The B3LYP (Becke, three-parameter, Lee–Yang–Parr) exchange-correlation functional with the Lee–Yang–Parr correlation functional at the 6-31G basis set in Gaussian 16 software[48] was used to calculate the properties of the $[BO_3F]$ unit in ABF and the $[BO_4]$ unit in LBO. The electronic wavefunction analysis is based on Multiwfn software[49]. In this paper, we performed first-principles calculations with the Vienna Ab initio Simulation Package (VASP)[50,51]. The exchange correlation potential and ion–electron interaction were treated in the Perdew–Burke–Ernzerhof functional together with the projector-augmented-wave method[52,53]. The outermost electrons of H-1s, B-2s2p, N-2s2p, O-2s2p and F-2s2p are considered as valence electrons. Structural relaxations used a quasi-Newton (BFGS) scheme until the residual forces on all atoms were less than 0.02 eV $Å^{-1}$ and, during geometry optimization, we used a plane-wave cut-off of 400 eV and Monkhorst–Pack meshes corresponding to a k-point spacing of 0.03 $Å^{-1}$. Static self-consistent calculations were then carried out with a 600-eV cut-off, an electronic convergence threshold of 1×10^{-7} eV and dense Monkhorst–Pack k-point mesh spanning less than 0.03 $Å^{-1}$. The Wannier functionals were constructed through a post-processing procedure using the output of VASP calculation and the corresponding orbitals type by the projection of all valence states in the unit cell were generated using Wannier90 (ref. 54). The optical properties of all compounds and the SHG contribution of each Wannier orbital were calculated. Here the plane-wave cut-off energy of 800 eV, threshold of 10^{-10} eV and the dense Monkhorst–Pack k-point grid is twice the static self-consistent-field calculation.

The length gauge formalism method was developed by Aversa and Sipe[55] to avoid unphysical divergences. At a zero frequency, the formula of second-order NLO coefficients can be derived as

$$\chi_{ijk}^{(2)} = \chi_{ijk}^{(2)}(\mathrm{VE}) + \chi_{ijk}^{(2)}(\mathrm{VH}) + \chi_{ijk}^{(2)}(\mathrm{TB})$$

in which

$$\chi_{ijk}^{(2)}(\mathrm{VE}) = \frac{e^3}{2\hbar^2 m^3} \sum_{vcc'} \int \frac{d^3\mathbf{k}}{4\pi^3} \mathrm{P}(ijk)\mathrm{Im}[p_{vc}^i p_{cc'}^j p_{c'v}^k] \left(\frac{1}{\omega_{cv}^3 \omega_{vc'}^2} + \frac{2}{\omega_{vc}^4 \omega_{c'v}} \right)$$

$$\chi_{ijk}^{(2)}(\mathrm{VH}) = \frac{e^3}{2\hbar^2 m^3} \sum_{vv'c} \int \frac{d^3\mathbf{k}}{4\pi^3} \mathrm{P}(ijk)\mathrm{Im}[p_{vv'}^i p_{v'c}^j p_{cv}^k] \left(\frac{1}{\omega_{cv}^3 \omega_{v'c}^2} + \frac{2}{\omega_{vc}^4 \omega_{cv'}} \right)$$

Here i, j and k are Cartesian components, v and v' denote valence bands, c and c' denote conduction bands and P (ijk) denotes full permutation and explicitly shows the Kleinman symmetry. Also, the contribution of virtual-electron (VE) and virtual-hole (VH) processes are dominant, whereas the two-band (TB) transition process was strictly proved to be zero[56]. Using unitary transformation, a set of Wannier functions $w_{n\mathbf{R}}(\mathbf{r}) = w_{n0}(\mathbf{r} - \mathbf{R})$ labelled by Bravais lattice vector $\mathbf{R}$ can be constructed by using Bloch eigenstates $\psi_{n\mathbf{k}}$ of band n (ref. 57) as

$$|w_{\alpha\mathbf{R}}\rangle = \frac{V}{(2\pi)^3} \int_{BZ} \mathrm{e}^{-\mathrm{i}\mathbf{k}\cdot\mathbf{R}} |w_{\alpha\mathbf{k}}\rangle \mathrm{d}\mathbf{k}^3$$

Within the chosen Wannier subspace, in terms of the projection coefficients $C_{n\mathbf{k}}^{\alpha}$, the Bloch state admits the expansion

$$|n\mathbf{k}\rangle = \sum_{\alpha} C_{n\mathbf{k}}^{\alpha} |w_{\alpha\mathbf{k}}\rangle$$

Here $|C_{n\mathbf{k}}^{\alpha}|^2$ represents the weight of $|w_{\alpha\mathbf{k}}\rangle$ in the nth valence-band-decomposed SHG $\chi_{ijk,n\mathbf{k}}^{(2)}$. Accordingly, the contribution of the total SHG $\chi_{ijk,w_\alpha}^{(2)}$ can be written[40]:

$$\chi_{ijk,w_\alpha}^{(2)} = \sum_{|n\mathbf{k}\rangle \in \{v\}} |C_{n\mathbf{k}}^{\alpha}|^2 \chi_{ijk,n\mathbf{k}}^{(2)}$$

Data availability

All data are available in the main text or the Extended Data.

42. Technical Committee: ISO/TC 172/SC9. *ICS: 31.260. Lasers and laser-related equipment — test methods for laser-induced damage threshold. Part 2: threshold determination. ISO 21254-2:2011.* (International Organization for Standardization, 2011).
43. Leviton, D. B., Madison, T. J. & Petrone, P. III Simple refractometers for index measurements by minimum-deviation method from far ultraviolet to near infrared. *Proc. SPIE* **3425**, 148–159 (1998).
44. Born, M. & Wolf, E. *Principles of Optics* 5th edn (Pergamon Press, 1975).
45. Maker, P., Terhune, R., Nisenoff, M. & Savage, C. Effects of dispersion and focusing on the production of optical harmonics. *Phys. Rev. Lett.* **8**, 21 (1962).
46. Jerphagnon, J. & Kurtz, S. K. Maker fringes: a detailed comparison of theory and experiment for isotropic and uniaxial crystals. *J. Appl. Phys.* **41**, 1667–1681 (1970).
47. Zhang, M. et al. Linear and nonlinear optical properties of $K_3B_6O_{10}Br$ single crystal: experiment and calculation. *J. Phys. Chem. C* **118**, 11849–11856 (2014).
48. Caricato, M., Frisch, A., Hiscocks, J. & Frisch, M. J. *Gaussian 09: IOps Reference* (Gaussian, Inc., 2009).
49. Lu, T. & Chen, F. W. Multiwfn: a multifunctional wavefunction analyzer. *J. Comput. Chem.* **33**, 580–592 (2012).
50. Kresse, G. & Furthmuller, J. F. Efficient iterative schemes for ab initio total-energy calculations using a plane-wave basis set. *Phys. Rev. B* **54**, 11169–11186 (1996).
51. Kresse, G. & Furthmuller, J. F. Efficiency of ab-initio total energy calculations for metals and semiconductors using a plane-wave basis set. *Comput. Mater. Sci.* **6**, 15–50 (1996).
52. Rappe, A. M., Rabe, K. M., Kaxiras, E. & Joannopoulos, J. D. Optimized pseudopotentials. *Phys. Rev. B* **41**, 1227–1230 (1990).
53. Perdew, J. P., Burke, K. & Ernzerhof, M. Generalized gradient approximation made simple. *Phys. Rev. Lett.* **77**, 3865–3868 (1996).
54. Pizzi, G. et al. Wannier90 as a community code: new features and applications. *J. Phys. Condens. Matter* **32**, 165902 (2020).
55. Aversa, C. & Sipe, J. E. Nonlinear optical susceptibilities of semiconductors: results with a length-gauge analysis. *Phys. Rev. B* **52**, 14636 (1995).
56. Zhang, B. B. et al. Simulated pressure-induced blue-shift of phase-matching region and nonlinear optical mechanism for $K_3B_6O_{10}X$ (X = Cl, Br). *Appl. Phys. Lett.* **106**, 031906 (2015).
57. Marzari, N. et al. Maximally localized Wannier functions: theory and applications. *Rev. Mod. Phys.* **84**, 1419–1475 (2012).

Acknowledgements This work was supported by the Strategic Priority Research Program of the Chinese Academy of Sciences (XDB0880000), the National Natural Science Foundation of

China (22335007, 22193044), the Tianshan Innovation Team Foundation (2022TSYCTD0005), the CAS Youth Interdisciplinary Team Foundation (JCTD-2022-19) and the Xinjiang Major Science and Technology Project (2021A01001).

Author contributions S.P. and X.L. conceptualized and designed the study. F.Z., Z.C., C.C., X.L. and S.P. developed the methodology. F.Z., Z.C., C.C., F.L., Z.Y., M.M. and X.H. conducted the investigation and data collection. F.Z., Z.C., C.C., F.L. and M.M. contributed to visualization and data analysis. F.Z. and S.P. secured funding acquisition. S.P. managed project administration. S.P. and X.L. supervised the research. F.Z., Z.C., C.C. and Z.Y. wrote the original draft. All authors critically reviewed, edited and approved the final manuscript.

Competing interests The authors declare no competing interests.

Additional information

Supplementary information The online version contains supplementary material available at https://doi.org/10.1038/s41586-025-10007-z.

Correspondence and requests for materials should be addressed to Shilie Pan.

Peer review information *Nature* thanks the anonymous reviewers for their contribution to the peer review of this work. Peer reviewer reports are available.

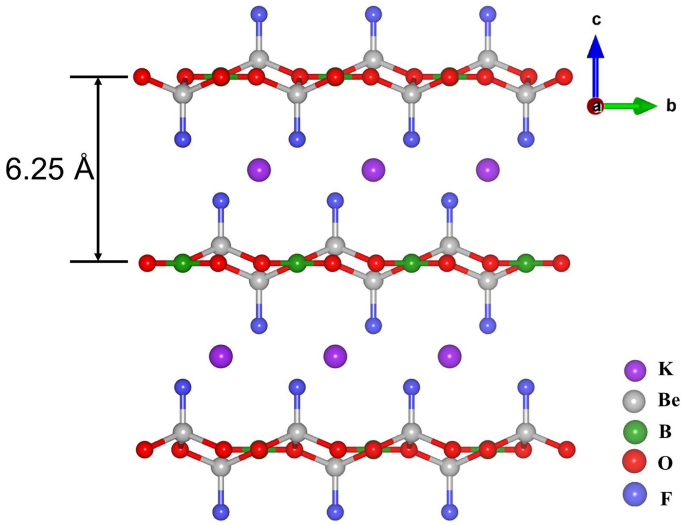

Extended Data Fig. 1 | Structure of KBBF featuring 2D $[Be_2BO_3F_2]_\infty$ layers with an interlayer distance of 6.25 Å. K^+ cations are located between the layers forming the final framework with ionic K–F bonds (not shown for clarity).

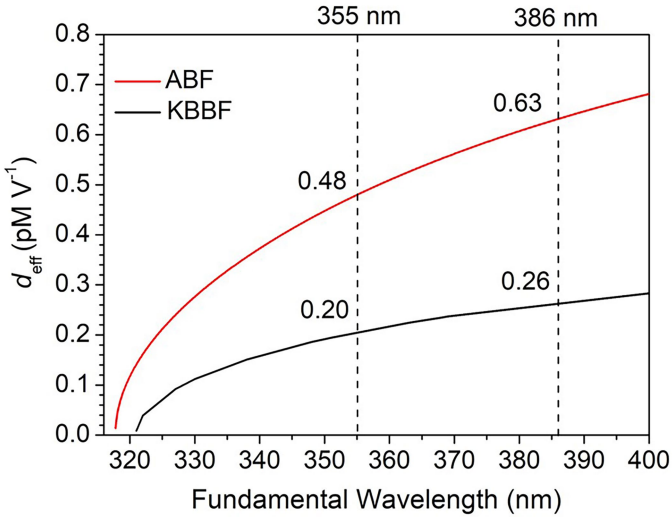

Extended Data Fig. 2 | Comparison of the effective NLO coefficients (d_{eff}) between ABF and KBBF at the fundamental wavelength range 310–400 nm. For type I phase-matching, d_{eff} (ABF) = $d_{32}\cos\varphi$, in which d_{32} = 1.09 pm V^{-1} based on the Maker fringe technique and d_{eff} (KBBF) = $d_{11}\cos\theta\cos3\varphi$, in which d_{11} = 0.47 pm V^{-1} (based on the Maker fringe technique[32]). The polar angle (θ) and azimuthal angle (φ) were calculated on the basis of the Sellmeier equations for ABF and KBBF (ref. 33), respectively. The weak dependence of d_{ij} on wavelength far from the cut-off edge was ignored. d_{eff} at 386 → 193 nm and 355 → 177.5 nm is highlighted by dashed lines.

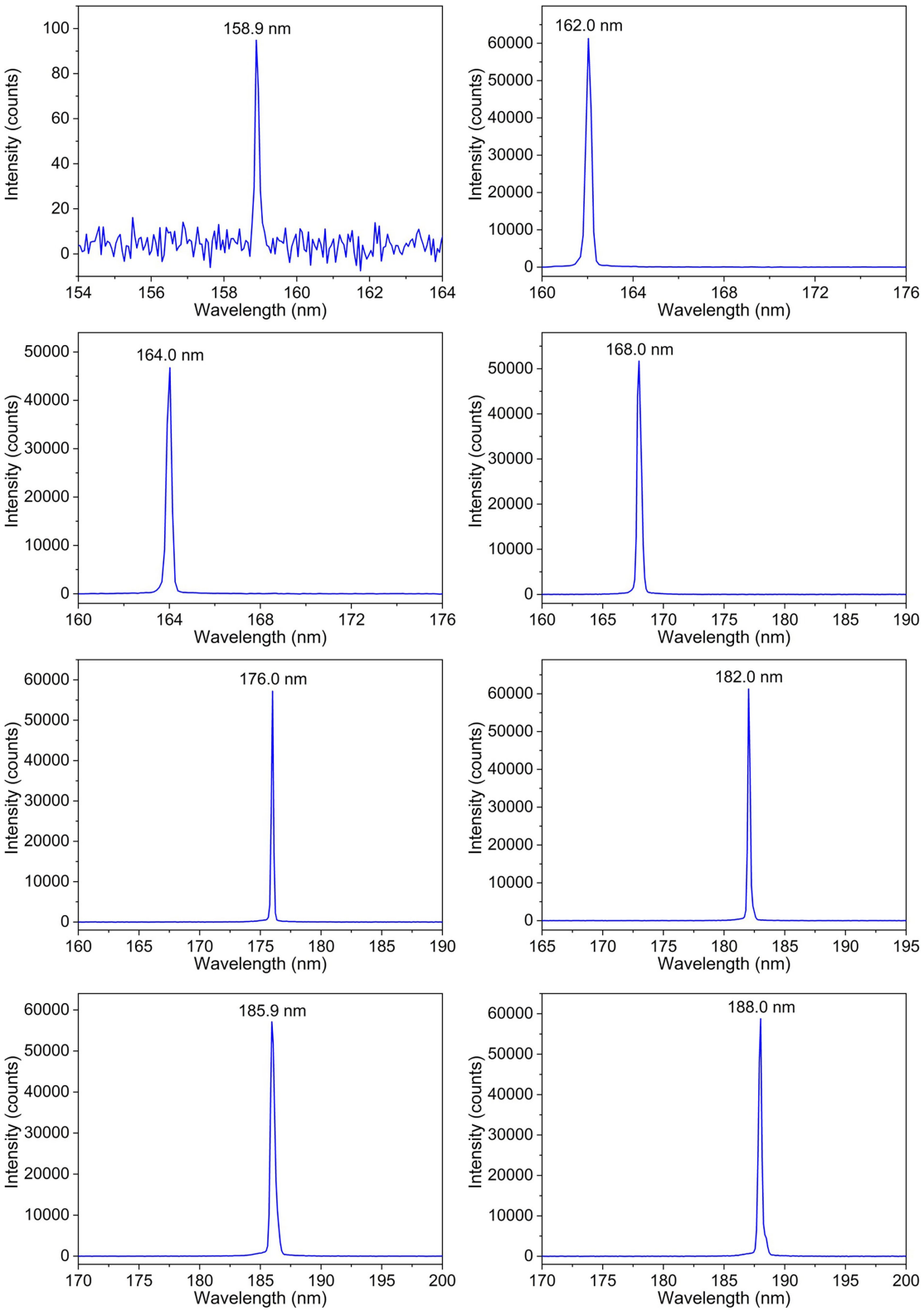

Extended Data Fig. 3 | Raw data of frequency-doubling light for 158.9–188.0 nm using the ABF device with (θ, φ) = (90°, 70°). *X*-axis: wavelength (nm); *Y*-axis: signal intensity (counts).

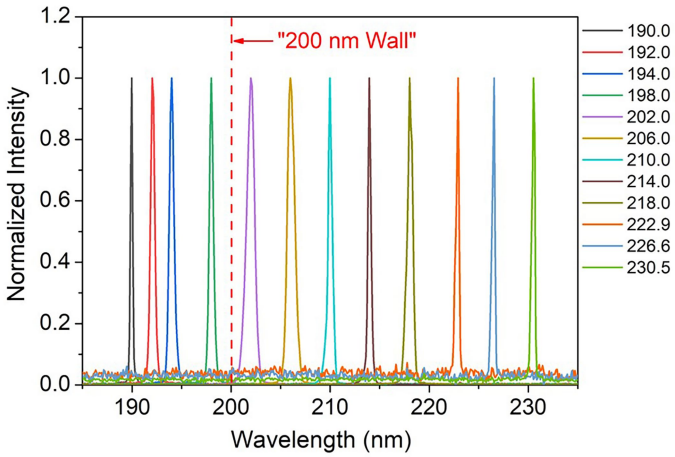

Extended Data Fig. 4 | Observation of frequency-doubling light for 190.4–230.5 nm using the ABF device with (θ, φ) = (90°, 40°). The dashed red line highlights breaking through the '200 nm wall'. Note that the SHG intensity is normalized for clarity.

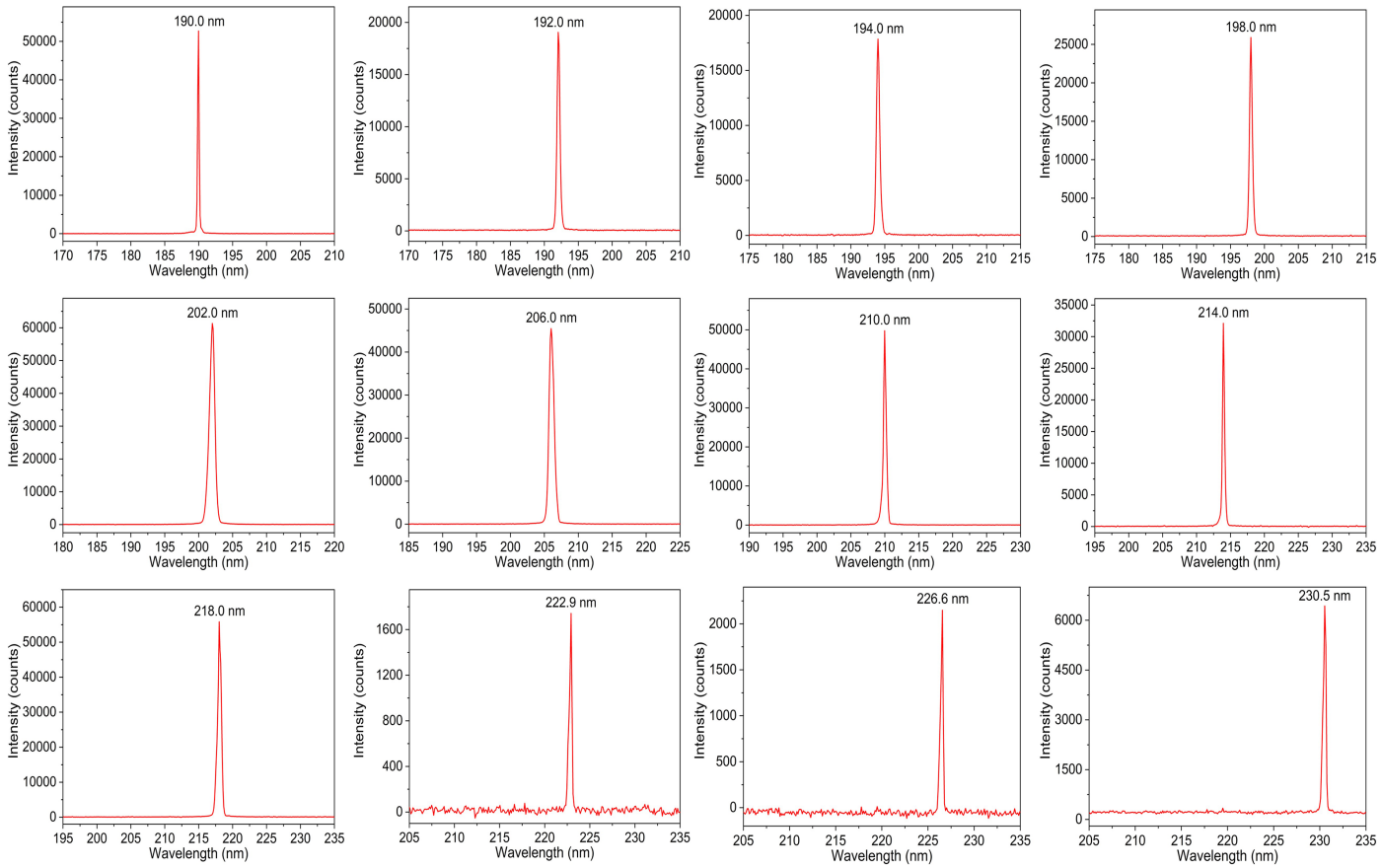

Extended Data Fig. 5 | Raw data of frequency-doubling light for 190.4–230.5 nm using the ABF device with (θ, φ) = (90°, 40°). *X*-axis: wavelength (nm); *Y*-axis: signal intensity (counts).

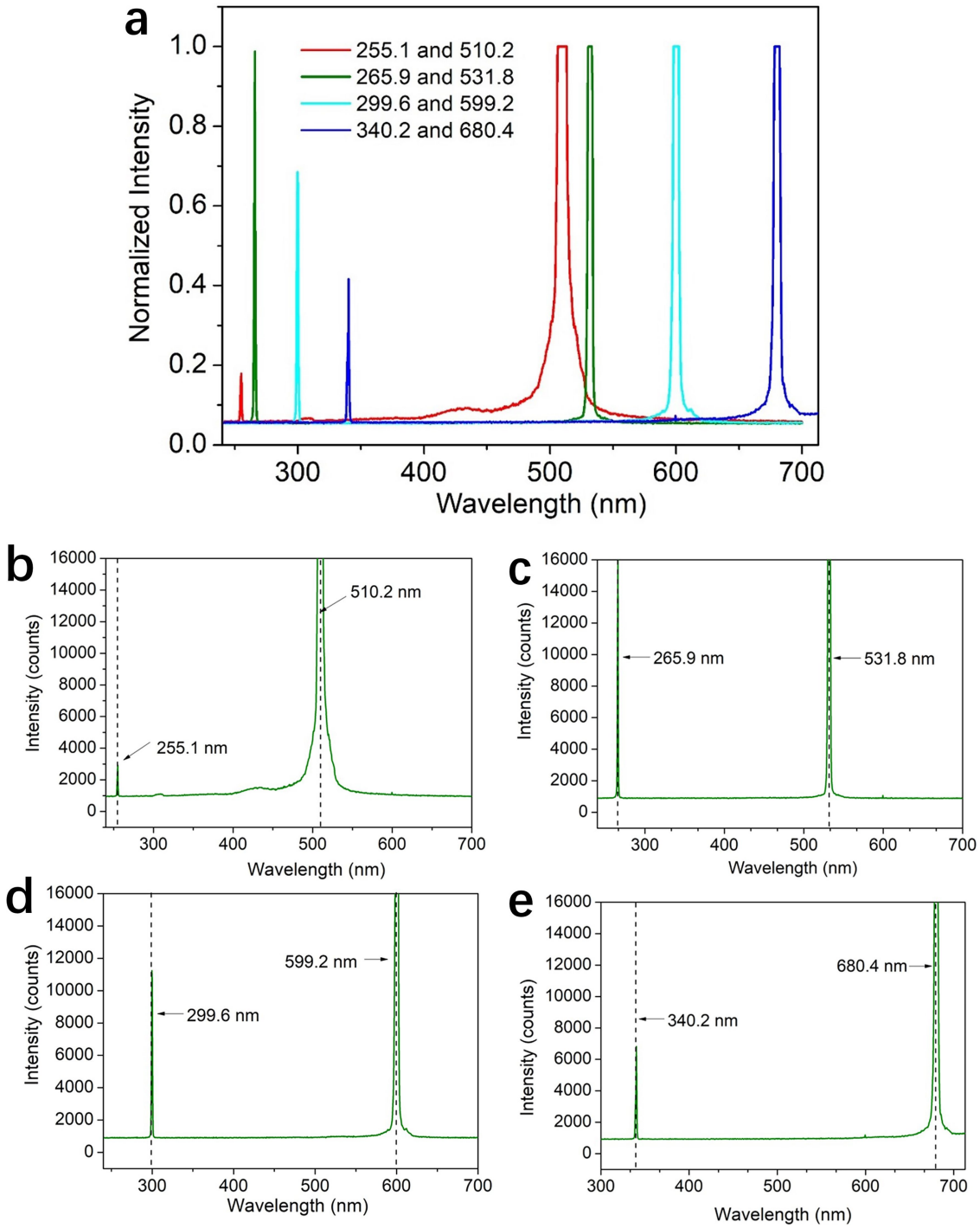

Extended Data Fig. 6 | Observation of frequency-doubling light from 255.1 to 340.2 nm using the ABF device with (θ, φ) = (90°, 0°). a, Normalized SHG intensity for clarity. **b**–**e**, Raw data of frequency-doubling light. Both fundamental and SHG light are highlighted by dashed lines in the figures. The fundamental wavelengths (510.2 nm, 531.8 nm, 599.2 nm and 680.4 nm) corresponding to the SHG signals are generated by a 355-nm-pumped BBO-OPO.

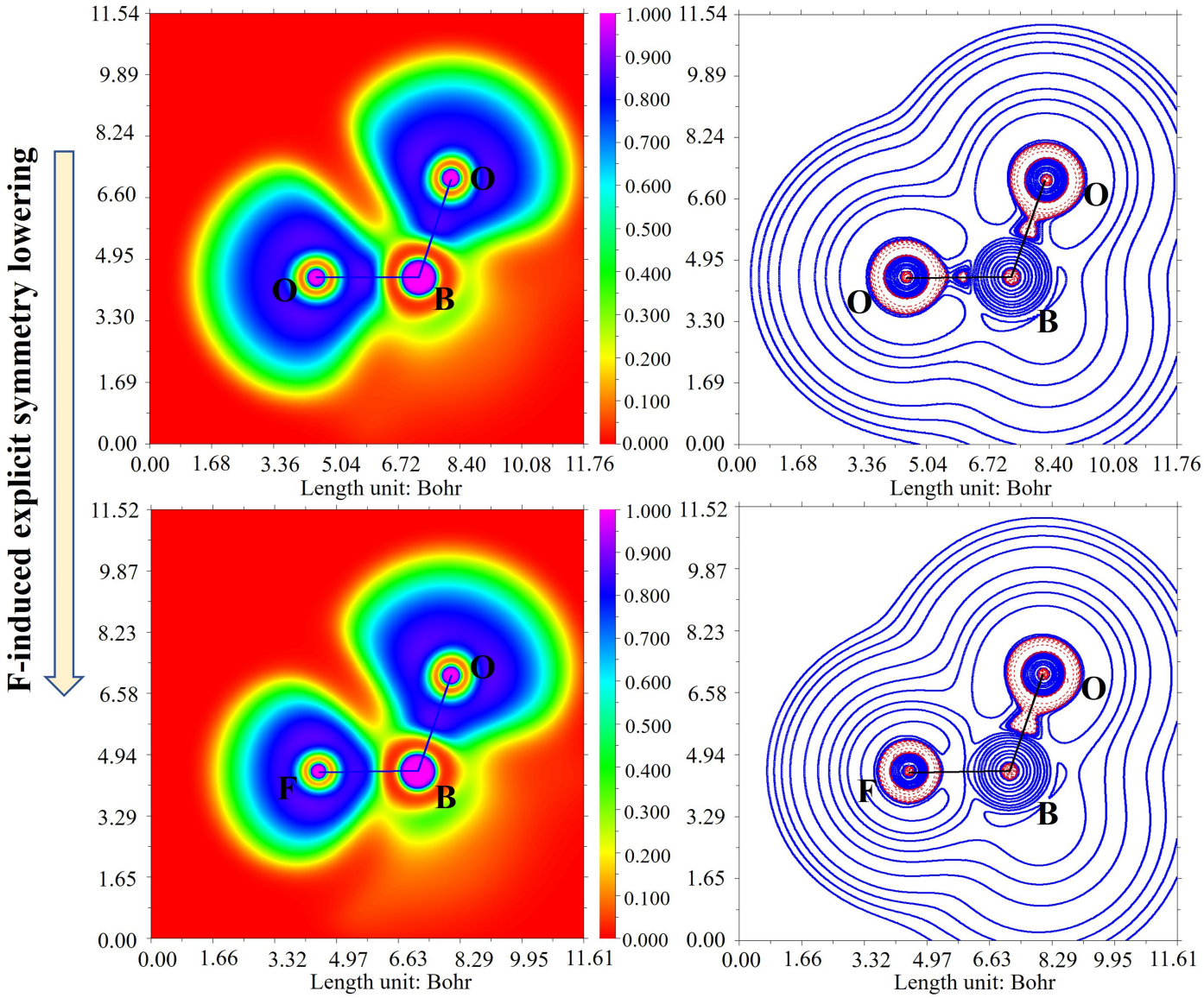

Extended Data Fig. 7 | Electron local function (ELF, left) and Laplacian charge density ($\nabla^2\rho$, right) of the [BO_4] unit in LBO (top) and the [BO_3F] unit in ABF (bottom). F induces explicit symmetry lowering in [BO_3F] relative to [BO_4], with differing Laplacian charge density as shown by the dashed red box.

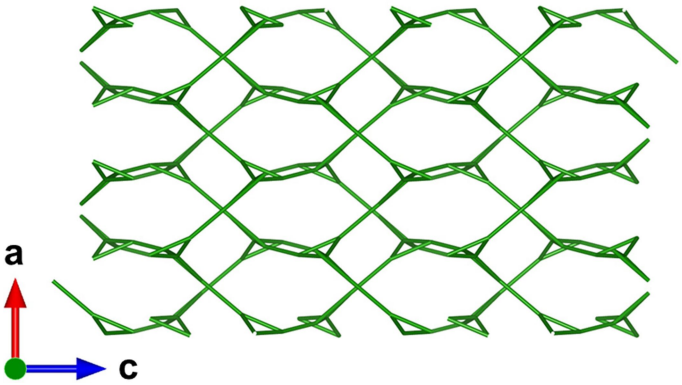

Extended Data Fig. 8 | Anionic framework structures with B as the node in $NH_4B_5O_8$. The structure data are derived from the Inorganic Crystal Structure Database (ICSD, 2025-1, version 5.4.0).

Extended Data Table 1 | Calculated effective SHG coefficients tensor (pm V^{-1}) and contribution of orbitals in the SHG coefficient d_{32} of ABF

Interaction orbitals	Contribution
NH_4-related orbitals (including NH_4···O hydrogen bond interaction orbital)	– 0.229 pm V^{-1} (23 %)
Boron and oxygen/fluorine related orbitals	– 0.773 pm V^{-1} (77 %)
Sum	– 1.002 pm V^{-1}

Percentages in parentheses represent the proportion of each orbital set's contribution to the total contribution of the SHG coefficient d_{32} of ABF.

Extended Data Table 2 | Comparison of key characteristics between KBBF and ABF

Characteristic	$KBe_2BO_3F_2$ (KBBF)	$NH_4B_4O_6F$ (ABF)
Single crystal growth characteristic	Layered growth habit, difficult to grow thick single crystal along the z-axis	Able to grow centimeter-scale single crystals
Device type	Prism-coupled device	Angle phase-matching device
Toxic BeO in growth raw material	Contains toxic BeO	Does not contain toxic BeO
Cutoff edge (nm)	147[18]	155.0
Birefringence@1064 nm	0.077[18]	0.117
Shortest experimentally achieved phase-matching SHG output wavelength (nm)	165[19]	158.9
Effective second-order NLO coefficient@386 nm	0.26	0.63
Effective second-order NLO coefficient@355 nm	0.20	0.48
Maximum SHG output energy@177.3nm (ns, 10 Hz) (mJ)	0.375[38]	4.8
SHG conversion efficiency@355 nm (%)	1.76[38]	5.9

KBBF data: cut-off edge/birefringence[18], shortest SHG wavelength[19], maximum SHG energy/conversion efficiency[38]. Unlabelled data are from this work.